

Chandra X-ray Observations of NGC 4258: Iron Absorption Lines from the Nucleus

A. J. Young² and A. S. Wilson²

Astronomy Department, University of Maryland, College Park, MD 20742

ABSTRACT

We report sub-arcsecond resolution X-ray imaging spectroscopy of the low luminosity active galactic nucleus of NGC 4258 and its immediate surroundings with the Chandra X-ray Observatory. NGC 4258 was observed four times, with the first two observations separated by one month, followed over a year later by two consecutive observations. The spectrum of the nucleus is well described by a heavily absorbed ($N_{\text{H}} \simeq 7 \times 10^{22} \text{ cm}^{-2}$, which did not change), hard X-ray power law of variable luminosity, plus a constant, thermal soft X-ray component. We do not detect an iron $K\alpha$ emission line with the upper limit to the equivalent width of a narrow, neutral iron line ranging between 94 and 887 eV (90% confidence) for the different observations. During the second observation on 2000-04-17, two narrow absorption features are seen with $> 99.5\%$ confidence at $\simeq 6.4$ keV and $\simeq 6.9$ keV, which we identify as resonant absorption lines of Fe XVIII – Fe XIX $K\alpha$ and Fe XXVI $K\alpha$, respectively. In addition, the 6.9 keV absorption line is probably variable on a timescale of ~ 6000 sec. The absorption lines are analyzed through a curve of growth analysis, which allows the relationship between ionic column and kinematic temperature or velocity dispersion to be obtained for the observed equivalent widths. We discuss the properties of the absorbing gas for both photo and collisionally ionized models. Given that the maser disk is viewed at an inclination $i = 82^\circ$, the gas responsible for the 6.9 keV absorption line may be in an inner disk, a disk-wind boundary layer or be thermal gas entrained at the base of the jet. The gas which gives rise to the photoelectric absorption may be the same as that which causes the 6.4 keV Fe $K\alpha$ absorption provided that the gas has a bulk velocity dispersion of a few thousand km s^{-1} . This is the first

¹Present address MIT Center for Space Research, 77 Massachusetts Avenue, Cambridge, MA 02139

²Adjunct Astronomer, Space Telescope Science Institute, 3700 San Martin Drive, Baltimore, MD 21218

detection of iron X-ray absorption lines in an extragalactic source with a nearly edge-on accretion disk, and this phenomenon is likely to be related to similar X-ray absorption lines in Galactic X-ray binaries with nearly edge-on accretion disks.

Subject headings: accretion, accretion disks — black hole physics — galaxies: active — galaxies: individual (NGC 4258) — galaxies: Seyfert — X-rays: galaxies

1. Introduction

The Seyfert 1.9 galaxy NGC 4258 (M 106) is a prime candidate for the study of low luminosity active galactic nuclei. The mass of the central black hole in NGC 4258 is well determined from position and velocity measurements of the H₂O maser emission which show a thin, slightly warped, accurately-Keplerian disk of radius 0.12 pc to 0.25 pc in orbit around a $(3.9 \pm 0.1) \times 10^7 M_{\odot}$ black hole (Nakai et al. 1993; Greenhill et al. 1995; Miyoshi et al. 1995; Herrnstein et al. 1999). Wilkes et al. (1995) have found strongly polarized, broad optical emission lines indicative of an obscured active nucleus. Early X-ray observations with Einstein (Cecil et al. 1992; Fabbiano et al. 1992) and ROSAT (Pietsch et al. 1994; Vogler & Pietsch 1999; Cecil et al. 1995) detected soft, extended X-ray emission, but could not penetrate the gas obscuring the nucleus. ASCA observations were the first to detect the active nucleus, which exhibited a power law spectrum of photon index $\Gamma \simeq 1.8$ and an absorption corrected 2 – 10 keV luminosity of $L_x = 4 \times 10^{40}$ erg s⁻¹ obscured by a column density of $N_H \simeq 1.5 \times 10^{23}$ cm⁻² (Makishima et al. 1994). The X-ray luminosity is a small fraction of the Eddington luminosity, $L_x/L_{\text{Edd}} \lesssim 3 \times 10^{-5}$. Subsequent ASCA observations have shown the nuclear luminosity to be variable on year-long timescales with L_x in the range $(0.4 - 1) \times 10^{41}$ erg s⁻¹ (Reynolds et al. 2000; Terashima et al. 2002; Ptak et al. 1999) while the photon index and column density have remained approximately constant. BeppoSAX observations revealed 100% continuum variability on a timescale of a few $\times 10^5$ s, and 10 – 20% variability on timescales as short as one hour (Fiore et al. 2001). Interesting variability has also been seen by ASCA in the 6.4 – 6.9 keV iron lines. In 1993, a narrow Fe line was seen at $6.66_{-0.07}^{+0.20}$ keV with an equivalent width (EW) of 180_{-64}^{+73} eV (Terashima et al. 2002), while in 1996, the Fe line energy had changed to $6.31_{-0.10}^{+0.09}$ keV with an EW of 54_{-27}^{+25} eV (Terashima et al. 2002). This change in line energy, by 0.35 keV, is significantly larger than the systematic uncertainty in the ASCA calibration (Iwasawa 2003). In a 1999 ASCA observation, a narrow iron line was observed at $6.45_{-0.07}^{+0.10}$ keV with an EW of 107_{-37}^{+42} eV (Reynolds et al. 2000). An XMM-Newton observation in 2000 constrained the EW of a 6.45 keV iron line to be < 45 eV (Pietsch & Read 2002), indicating that the iron line had

weakened significantly since the 1999 ASCA observation (a ~ 100 eV EW narrow iron line would have easily been detected in the XMM-Newton observation).

We have obtained a series of Chandra observations to study various aspects of NGC 4258. At 7.2 Mpc (Herrnstein et al. 1999) $1'' = 35$ pc, and we take the Galactic hydrogen column towards NGC 4258 to be $N_{\text{H}} = 1.19 \times 10^{20} \text{ cm}^{-2}$ (Murphy et al. 1996).

2. Observations and Reduction

NGC 4258 was observed by Chandra on four separate occasions with ACIS-S (Table 1). The first observation on 2000-03-08 had a duration of 2.9 ksec, with a 128 row sub-array and alternating 0.4 sec and 0.1 sec frame-times, in order to obtain an approximate count rate and assess the effects of pile-up. The second observation on 2000-04-17 had a duration of 13 ksec with a full frame and 3.2 sec frame-time, primarily to study the “anomalous arms” of NGC 4258 (Wilson et al. 2001, hereafter WYC); the nucleus suffers from the effects of pile-up. The third observation on 2001-05-28 had a duration of 20 ksec with a full frame and 3.2 sec frame-time, again to study the anomalous arms, and the nucleus again suffers from the effects of pile-up. The fourth observation, taken immediately after the third, on 2001-05-29 had a duration of 7 ksec with a 128 row sub-array and a 0.4 sec frame-time to mitigate the effects of pile-up and to study the nucleus of NGC 4258.

The latest gain files were applied to the data and background flares were filtered out by excluding data from those times during which the background (i.e. source-free regions on the S3 chip) count rate was $> 3\sigma$ above or below the mean background count rate. For the 2.9 ksec duration observation, we used a dead-time correction (DTCOR) of 0.552 to calculate the exposure time of the 0.4 sec frames. The resulting exposure times are listed in Table 1. We shall refer to the 4 observations as the 1.6 ksec, 13 ksec, 20 ksec and 7 ksec exposures respectively. Note that because the 0.4 sec frame-time 1.6 ksec exposure was taken in an alternating mode, the 1.6 ksec of exposure time is spread over the 2.9 ksec duration of the observation. CIAO 2.2.1 with CALDB 2.17 were used, and the spectra were analyzed using XSPEC 11.2 (Arnaud 1996). To obtain spectra of the nucleus, counts were extracted from circular apertures of radius $1''.5$ centered on the brightest pixel, and background counts were extracted from an annulus of inner radius $4''$ and outer radius $10''$ also centered on the nucleus. The spectra were grouped to ≥ 15 counts per bin and the χ^2 statistic was used to compare models to the data. The confidence region for a model parameter was determined by varying that parameter until the χ^2 value, minimized by allowing all of the remaining free parameters to vary, was equal to the best fit value plus $\Delta\chi^2$ where $\Delta\chi^2 = 2.706, 6.635$ and 7.879 for the 90% 99% and 99.5% confidence regions for a single interesting parameter,

respectively. Unless stated otherwise 90% confidence regions have been used.

When analyzing spectra of the nucleus taken with a 3.2 sec frame-time it is important to correct for the effects of pile-up (the 0.4 sec frame-time observations do not require pile-up correction), and we used the pile-up correction routine of Davis (2001) that is incorporated into the XSPEC software package. We find the grade morphing parameter α (the fraction of “good grades” given by p piled-up photons is $\propto \alpha^{(p-1)}$) to be $\alpha = 0.41_{-0.07}^{+0.06}$ for the 20 ksec data set and $\alpha = 0.43_{-0.03}^{+0.03}$ for the 13 ksec data set.

3. X-ray Morphology

The 3.2 s frame-time observations of 2000-04-17 and 2001-05-28 have been combined to produce the grey scale image shown in Fig. 1. Here we concentrate on the nucleus and its immediate environment, and do not discuss the much larger scale “anomalous arms” (see WYC). As noted by WYC and by Pietsch & Read (2002), there is a weaker source 2.5 southwest of the nucleus. Soft, diffuse emission is seen to extend to the northwest and southeast of the nucleus, and this emission is the beginning of the “anomalous arms”. Comparing the spatial distribution of the 3 – 8 keV counts from the nucleus in the 2001-05-29 observation, which does not suffer from pile-up, with a theoretical point spread function at 6.4 keV, we find that the hard X-ray nucleus is unresolved.

4. X-ray Light Curves

X-ray light curves of the nucleus of NGC 4258 in 450 s bins are shown in Fig. 2. The background count rate is negligible ($< \text{few} \times 10^{-4} \text{ cts s}^{-1}$) and has not been subtracted. The 3.2 sec frame-time data sets have been corrected for the effects of pile-up, using the continuum models given in Section 5.1. The light curves show 10 – 14% rms variability on short timescales and $\gtrsim 20\%$ variability on year-long timescales between the first and last observations (panels a and d, neither of which is affected by pile-up). One of the effects of moderate to severe pile-up is to reduce the sensitivity of the observed count rate to changes in the actual count rate (i.e., as the actual count rate increases the observed count rate increases at a much slower rate). This effect adds a systematic error to our determinations of the un-piled mean count rates (panels b and c) as well as reducing the observed amplitude of short timescale variability. This systematic error is difficult to estimate, but may be as large as a few $\times 10\%$.

5. X-ray Spectra

5.1. Nucleus

5.1.1. Continuum Spectrum

Initially we studied the 2001-05-29 observation (which has an exposure time of 7 ksec and a frame-time of 0.4 sec) because it is the highest S/N observation not affected by pile-up. Two components are required to describe the spectrum of the nucleus: i) a low energy component below ~ 2 keV, such as a 1 keV bremsstrahlung absorbed by the Galactic column, and ii) a heavily absorbed ($N_{\text{H}} \simeq 7 \times 10^{22} \text{ cm}^{-2}$) high energy component above ~ 2 keV, such as a hard power law of photon index $\Gamma \simeq 1.4$ or a very hot bremsstrahlung with a temperature $\gtrsim 20$ keV. We then modeled the other data sets in a similar manner, correcting for pile-up as necessary. Table 2 summarizes our models of the continuous spectra of the nucleus for the different observations, and Fig. 3 shows a model fit to the 2001-05-28 data set. For each of these observations, the soft X-ray component is the same while the hard X-ray component declined from 2000 to 2001. During this variation, the intrinsic absorbing column density and photon index of the hard component remained constant (Table 2). The models presented here assume absorption by a single column of neutral gas. If the absorber is ionized then a higher column density may be permitted (see discussion in Sections 6.1.1 and 6.1.2). If a partial covering model is used the best fit has a covering fraction of $\gtrsim 99\%$ and parameters very similar to our single absorber fits; the uncovered fraction, $\lesssim 1\%$ of the nucleus, accounts for the observed soft emission. It is also possible for an additional absorption component to be added to our models; $\sim 40\%$ of the nucleus may be absorbed by $N_{\text{H}} \sim 7 \times 10^{22} \text{ cm}^{-2}$ while $\sim 60\%$ of the nucleus may be absorbed by an additional $N_{\text{H}} \sim 8 \times 10^{23} \text{ cm}^{-2}$, and this model requires a softer power law, with $\Gamma \sim 1.9$. In addition, an arbitrary amount of complete obscuration may be present that we cannot constrain. Our decision to use a single column density is the most conservative approach and this column density is a lower limit to the true column density.

5.1.2. Iron Emission Lines

We now focus our attention on the spectrum in the region of the Fe $K\alpha$ lines. The ratios of the data to the best fitting power law models above 5 keV are shown in Fig. 4, in which no strong iron $K\alpha$ emission lines are apparent. If a narrow, neutral iron $K\alpha$ emission line at a rest frame energy of 6.4 keV is added to the model, the upper limit to the EW of such a line is ranges between 94 and 887 eV (90% confidence) for the different observations (see

Table 3). If the data are grouped to have ≥ 10 or ≥ 3 counts per bin, there is tentative evidence of iron $K\alpha$ emission lines in the first observation and the last two observations at the energies expected for neutral and H-like iron, although these features have low statistical significance.

5.1.3. Iron Absorption Lines

During the 2000-04-17 observation two strong absorption features are seen at NGC 4258 rest frame energies of $6.41_{-0.06}^{+0.05}$ keV and $6.87_{-0.06}^{+0.09}$ keV, with equivalent widths of -166 eV and -215 eV, respectively (see Fig. 4 and Table 3; the heliocentric redshift of NGC 4258 is $z = 0.00155$ (Cecil et al. 1992)). These absorption lines at 6.41 keV and 6.87 keV are both statistically significant at $> 99.5\%$ confidence (Table 3). An F-test may be used to quantify the improvement to the simple power law model when the absorption features are added. The power law model has χ^2 / degrees of freedom (dof) of $115.8 / 101$. Adding a single absorption line at 6.41 keV (the energies of all absorption features discussed here have been left as free parameters) to the power law model gives an improvement of $\Delta\chi^2 / \Delta \text{dof} = 12.9 / 2$, which is significant with 99.5% confidence. Adding a single absorption line at 6.87 keV to the power law model gives an improvement of $\Delta\chi^2 / \Delta \text{dof} = 7.7 / 2$, which is significant with 96.2% confidence, although the absence of the 6.41 keV line is so significant that it affects the continuum fit in the iron line band. If we add the 6.87 keV line to the power law plus 6.41 keV line model we find an improvement with the addition of the 6.9 keV line of $\Delta\chi^2 / \Delta \text{dof} = 11.6 / 2$, which is significant with 99.5% confidence. If we compare the power law model to the model with two absorption lines we find $\Delta\chi^2 / \Delta \text{dof} = 23.5 / 4$, significant at $> 99.9\%$. Only three of our observations have sufficient signal-to-noise ratio to detect absorption lines of this strength, and if we assume they are either “cold” lines at ~ 6.4 keV or “hot” lines at ~ 6.9 keV, this give us only six “chances” to see a strong iron absorption feature, so the presence of absorption lines at these energies in this data set is significant with at least 99.5% confidence. Continuing to assume the absorption lines are subject to only the redshift of NGC 4258, the 6.41 keV line is consistent with either of or a blend of the $n = 1 \rightarrow 2$ resonance lines of Fe XVIII and Fe XIX at 6.43 and 6.46 keV, respectively (the energy expected for Fe XX is 6.50 keV and inconsistent with the data, while ionization states below Fe XVIII do not have an L-shell vacancy). The feature at 6.87 keV is probably the $n = 1 \rightarrow 2$ resonance line of Fe XXVI at 6.97 keV (the energy expected of Fe XXV is 6.70 keV which is inconsistent with the measured value).

There is no evidence of a strong iron K absorption edge at 7.8 keV (from Fe XVIII; we use the edge energies given by Verner & Yakovlev 1995), 7.9 keV (from Fe XIX), with a limit

of $\tau_{\text{edge}} \lesssim 0.5$. We are insensitive to an absorption edge at 9.3 keV (from Fe XXVI).

If the 2000-04-17 observation is divided into two consecutive segments, each 6 ksec in duration, we can attempt to investigate any short timescale variability of the absorption features. The spectra of the iron line region for each of these segments is shown in Fig. 5. A strong absorption line is seen at ~ 6.9 keV in the first segment, but has disappeared in the second segment 6000 sec later. In the first segment, the addition of a narrow absorption line at $6.95_{-0.12}^{+0.22}$ keV to the continuum model is statistically significant with $> 99.5\%$ confidence (see Table 3). In the second segment, the addition of an absorption feature at 6.9 keV to the continuum model does not improve the fit at all. If the model of the second segment includes an absorption line at 6.95 keV, identical to that observed in the first segment, we find that removing this line improves the quality of the fit with $> 95\%$ confidence. These considerations indicate that the narrow absorption feature at 6.9 keV in the first segment is real and that it is significantly weaker in the second segment. The absorption feature at 6.4 keV is seen during both segments; in the first, it is significant at only the $> 90\%$ confidence level, but is marginally stronger in the second segment where it is statistically significant at $> 99.5\%$ confidence.

5.2. Off-nuclear Source

The spectrum of the off-nuclear source taken from the 20 ksec observation on 2001-05-28 is well described by an absorbed power law. The intrinsic column density is $N_{\text{H}} = 4.3_{-1.6}^{+2.8} \times 10^{21} \text{ cm}^{-2}$, the power law photon index is $\Gamma = 1.8_{-0.4}^{+0.5}$, and the unabsorbed 2 – 10 keV luminosity is $L_{\text{x}} = 6.1 \times 10^{38} \text{ erg s}^{-1}$ (assuming the source is in NGC 4258). These parameters are consistent with those found by WYC from the observation on 2000-04-17.

6. The Fe Absorption Lines

6.1. Curve of Growth Analysis

In order to see a strong absorption line, the solid angle of the resonantly scattering material as seen by the central X-ray source must be small, otherwise the absorption line would be “filled in” by emission lines. We thus imagine the absorbing material as a “blob” of gas, and use the strength of an absorption line to estimate the column density of the iron ion responsible for the absorption. Following the method described by Kotani et al. (2000) (also see Spitzer 1978), the equivalent width (EW), W_{ν} , of a resonance line at a frequency ν

is given by

$$W_\nu = \int_0^\infty \{1 - e^{-N_{\text{Fe}}\sigma(\nu)}\} d\nu \text{ [Hz]} \quad (1)$$

where N_{Fe} is the column density of the iron ion in question and $\sigma(\nu)$ is the cross section of that ion at a frequency ν . If the ions obey a Maxwell-Boltzmann distribution, then $\sigma(\nu)$ has a Voigt profile that depends on the temperature of the blob, being broader at a higher temperature. If the energy distribution of the ions is dominated by turbulence or bulk motion, then the appropriate turbulent or bulk velocity dispersion is used in place of the temperature-dependent velocity dispersion. The oscillator strengths and Einstein coefficients required to determine the cross sections were taken from Verner et al. (1996) for Fe XXVI $K\alpha$ and Behar & Netzer (2002) for Fe XVIII and Fe XIX $K\alpha$. Equation (1) was integrated for different values of N_{Fe} giving the “curve of growth” (W_ν vs. N_{Fe}), shown in Fig. 6 for Fe XXVI (cf. Kotani et al. 2000, their Fig. 3), Fe XVIII and Fe XIX $K\alpha$ (the absorption line at ~ 6.4 keV may be a blend of Fe XVIII and Fe XIX, and here we assume that the iron ions are equally divided between Fe XVIII and Fe XIX). From Fig. 6, we note that the large EW of the absorption lines we see ($-166 - -215$ eV; Table 3) can correspond to a broad range of iron column densities depending on the kinematic temperature of the blob. For example, the column density of Fe XXVI required to produce a 215 eV EW absorption line decreases from $N_{\text{Fe XXVI}} = 6 \times 10^{21} \text{ cm}^{-2}$ at a temperature of $kT \leq 100$ keV (equivalent to a 1σ line of sight velocity dispersion of the iron ions of $\Delta v \sim 4.1 \times 10^7 \text{ cm s}^{-1}$) to $N_{\text{Fe XXVI}} = 5 \times 10^{18} \text{ cm}^{-2}$ at $kT = 10,000$ keV (equivalent to a 1σ velocity dispersion of the iron ions of $\Delta v \sim 4.1 \times 10^8 \text{ cm s}^{-1}$).

A complication is that, while we see strong absorption lines from a blend of Fe XVIII – Fe XIX and from Fe XXVI, we do not see a strong absorption line from Fe XXV. For a single temperature, collisionally ionized or photoionized plasma, such is not possible (see Arnaud & Raymond 1992; Krolik & Kallman 1984, respectively), so there must be two distinct blobs with different ionization states. Since the absorption line from Fe XVIII – Fe XIX did not vary during the 13 ksec exposure while the Fe XXVI absorption line did vary, it is likely that the ~ 6.4 keV absorption line originates in cooler gas at larger radii. We shall, therefore, assume that the ~ 6.4 keV and ~ 6.9 keV absorption lines originate in spatially distinct blobs. We also assumed that the ion velocities within each absorbing blob are well described by a Maxwell-Boltzmann distribution since the CCD-resolution spectra provide little information about the line profile. This need not be the case, and the absorption lines may be made up of a number of individual components some of which may be saturated while others are unsaturated (equivalently the blob may be made up of sub-blobs of different column densities and velocity dispersions). It is difficult to quantify how these differences would affect our analysis, but the velocity dispersion that we derive can be thought of as a column density weighted mean velocity dispersion of (and within) the sub-blobs.

In the following, we derive some physical parameters of the “blobs”. In particular, we are interested in their opacity in the 2 – 5 keV region, as this is the range of the spectrum from which the equivalent hydrogen absorbing column of $N_{\text{H}} = 7 \times 10^{22} \text{ cm}^{-2}$ was derived, assuming the gas is neutral and of solar abundance (Section 5.1.1).

6.1.1. Photoionized Plasma

We first investigate the blob responsible for the Fe XXVI $K\alpha$ absorption line. For $W_{\nu} = -215 \text{ eV}$ (Table 3), our curve of growth analysis indicates that $N_{\text{Fe XXVI}} \gtrsim 6 \times 10^{18} \text{ cm}^{-2}$ (see Fig. 6) and, if the iron abundance is equal to the solar value of 3.5×10^{-5} Fe ions per hydrogen nucleus (Anders & Grevesse 1989), this column corresponds to $N_{\text{H}}(\text{ionized}) \gtrsim 2 \times 10^{23} \text{ cm}^{-2}$. If the gas in this blob is photoionized so that the ionization state of iron is dominated by Fe XXVI, an ionization parameter $\xi = L_{\text{x}}/(n_e R^2) \simeq 3000 \text{ erg cm s}^{-1}$ is required (Kallman & McCray 1982), where n_e is the electron density and R is the distance of the blob from the ionizing source. The plasma temperature corresponding to $\xi = 3000 \text{ erg cm s}^{-1}$ is $T \simeq 3 \times 10^6 \text{ K}$, and $\simeq 60\%$ of the iron ions are in the form of Fe XXVI, with the remainder being evenly split between Fe XXV and Fe XXVII (Kallman & McCray 1982). The X-ray opacity of such a gas is reduced by a large factor below the Fe K edge (Krolik & Kallman 1984) and hence a column density of $N_{\text{H}}(\text{ionized}) \gtrsim 2 \times 10^{23} \text{ cm}^{-2}$ is consistent with $N_{\text{H}}(\text{obs}) = 7 \times 10^{22} \text{ cm}^{-2}$. If we consider instead the stronger 6.9 keV line seen during the first segment of the 2000-04-17 observation the column density requirements are increased by a factor of a few, and are still consistent with $N_{\text{H}}(\text{obs})$.

We now turn our attention to the blob producing the Fe $K\alpha$ 6.4 keV absorption feature from a blend of Fe XVIII–Fe XIX $K\alpha$. For $W_{\nu} = -166 \text{ eV}$ (Table 3) our curve of growth analysis indicates that $N_{\text{Fe}} \gtrsim 10^{19} \text{ cm}^{-2}$ (see Fig. 6) and, if the iron abundance is equal to the solar value, this corresponds to $N_{\text{H}}(\text{ionized}) \gtrsim 3 \times 10^{23} \text{ cm}^{-2}$. A photoionized plasma with an ionization parameter of $\xi \simeq 100 \text{ erg cm s}^{-1}$ has almost all of its iron ions evenly distributed between Fe XVIII and Fe XIX (Kallman & McCray 1982, model 1). The plasma temperature corresponding to $\xi = 100 \text{ erg cm s}^{-1}$ is $T \simeq 10^5 \text{ K}$. From 2 to 5 keV the opacity is $\simeq 3$ times smaller than that of a neutral gas (Krolik & Kallman 1984). Given the approximations inherent to our analysis, the required column density of $N_{\text{H}}(\text{ionized}) \gtrsim 3 \times 10^{23} \text{ cm}^{-2}$ is consistent with the equivalent hydrogen column density for neutral gas ($N_{\text{H}} = 7 \times 10^{22} \text{ cm}^{-2}$ – see Table 2) needed to account for the observed *photoelectric* absorption. This consistency, however, requires a very high kinematic temperature of $kT \gtrsim 1000 \text{ keV}$, which presumably represents bulk motion with a 1σ line of sight velocity dispersion of the iron ions of $\Delta v \gtrsim 1.3 \times 10^8 \text{ cm s}^{-1}$. We conclude that the gas responsible for the observed

photoelectric absorption may be the same as that responsible for the 6.4 keV Fe absorption line.

6.1.2. Collisionally ionized Plasma

We first consider the blob responsible for the Fe XXVI $K\alpha$ absorption line. If the absorbing gas is collisionally ionized, the ionic fraction of Fe XXVI is maximal at a temperature $T \simeq 10^8$ K (Arnaud & Raymond 1992), and such a plasma will have negligible opacity in the 2 – 5 keV band (Krolik & Kallman 1984).

Considering next the blob responsible for the ~ 6.4 keV absorption line, the ionic species Fe XVIII – Fe XIX have maximal fractions at a temperature of $T \simeq 10^7$ K (Arnaud & Raymond 1992) and such a plasma will have a negligible opacity at energies $\lesssim 2$ keV, and roughly an order of magnitude lower opacity than neutral gas in the 2 – 5 keV band (Krolik & Kallman 1984). If such a blob is responsible for *both* the observed photoelectric absorption and the -166 eV EW absorption line at 6.4 keV, a kinematic temperature of $kT \sim 1000$ keV (equivalent to a 1σ line of sight velocity dispersion of the iron ions of $\Delta v \sim 1.3 \times 10^8$ cm s $^{-1}$) is needed. In this case, the absorbing gas could be in collisional equilibrium at 10^7 K, with the above value of Δv representing the turbulent or bulk outflow velocity. Thus, again, it is possible that the gas responsible for the observed photoelectric absorption is the same as that which gives the Fe $K\alpha$ absorption line at 6.4 keV.

We emphasize that all other observations of NGC 4258 made by us (Table 3) and others (Section 1) have found either no Fe lines or Fe lines in emission. Thus the spectrum is clearly variable (cf. Terashima et al. 2002). If we adopt the conclusion that the gas responsible for the Fe $K\alpha$ 6.4 keV absorption seen on 2000-04-17 is indeed the same as that which causes the photoelectric absorption, then the variability at 6.4 keV would result from variability in the emission line, since the photoelectric absorbing column density appears to be constant (Table 2 and papers cited in Section 1).

6.1.3. Nature of Absorbing Plasma

Since our line of sight to the nucleus grazes the surface of the thin, masing disk of NGC 4258 (inclination $i = 82^\circ \pm 1^\circ$; Herrnstein et al. 1999), the absorbing blobs may be part of a disk-wind boundary layer or an outflow. The absence of strong iron $K\alpha$ emission is consistent with a hot, low radiative efficiency, advection dominated accretion flow (ADAF; e.g., Narayan & Yi 1994; Abramowicz et al. 1995) with a lower limit to the radius of an outer

thin disk of approximately $100R_G$ (Reynolds et al. 2000). Such accretion flows may show strong outflows (Blandford & Begelman 1999) or convection (Quataert & Gruzinov 2000; Narayan et al. 2000) and the ionized absorbing “blobs” we have found in NGC 4258 may be inhomogeneities in such a flow with high turbulent velocities (to account for the large equivalent widths of the absorption lines – see Fig. 6). The short-timescale variability of the 6.9 keV absorption line (Section 5.1.3) might result from absorption by a blob at $\sim 10R_G$ which corresponds to a dynamical timescale of ~ 6000 sec.

The X-ray emission from the nucleus of NGC 4258 may originate from the base of the jet. As gas transitions from the ADAF to the jet it is shock heated, and the X-ray continuum emission may be synchrotron self-Compton emission from the accelerated electrons (Yuan et al. 2002). The mass ejection process may be unstable and the absorption lines we see could be from blobs of cooling thermal gas entrained in the jet outflow.

It is also very interesting to note that similar X-ray absorption features have been seen from the Galactic black hole or neutron star binaries GRO J1655-40 (Ueda et al. 1998; Yamaoka et al. 2001), Circinus X-1 (Brandt & Schulz 2000; Schulz & Brandt 2002), GRS 1915+105 (Kotani et al. 2000; Lee et al. 2002), GX 13+1 (Ueda et al. 2001), MXB 1659-298 (Sidoli et al. 2001), X 1624-490 (Parmar et al. 2002) and X 1254-690 (Boirin & Parmar 2003), all of which have high inclination accretion disks ($i \simeq 60^\circ - 80^\circ$, with the exception of GX 13+1 for which the inclination is not known). If a high inclination is required to produce a strong absorption line, as is suggested by these observations, then NGC 4258 is an important galaxy to study the connection between accretion disks in AGN and Galactic systems.

7. Conclusions

Our four Chandra observations of the low luminosity active galactic nucleus of NGC 4258 have shown:

- i) The continuum spectrum contains a component below 2 keV, such as 1 keV thermal emission absorbed by the Galactic column, plus a component above 2 keV, which is well described by a hard power law ($\Gamma = 1.4$) absorbed by an equivalent hydrogen column of $N_H = 7 \times 10^{22} \text{ cm}^{-2}$.
- ii) The soft component of the continuum spectrum does not vary, while the flux of the hard component declined from March/April 2000 to May 2001. During this decline, the intrinsic absorbing column density and photon index of the hard component remained constant (Table 2).

iii) We do not detect an iron $K\alpha$ emission line, with the upper limit to the EW of a narrow, neutral iron line ranging between 94 and 887 eV (90% confidence) for the different observations (Table 3). In the second observation (on 2000-04-17) absorption lines are seen at 6.4 and 6.9 keV that are statistically significant with $> 99.5\%$ confidence. There is evidence that the absorption line at 6.9 keV varied on a timescale of 6000 secs.

iv) We argue that the absorption lines are Fe $K\alpha$ resonant absorption, with that at 6.4 keV by Fe XVIII – Fe XIX, and that at 6.9 keV by Fe XXVI ions. A curve of growth analysis has been performed for each line in order to obtain the relationship between the kinematic temperature and the ionic column for the observed equivalent width.

v) Given that the maser disk is viewed at an inclination $i = 82^\circ$, we suggest that the 6.9 keV absorbing gas may be in an inner disk, a disk-wind boundary layer or be thermal gas entrained at the base of the jet.

vi) The gas responsible for the 6.4 keV absorption line may be photoionized or collisionally ionized. In each case, either the ionization temperature is lower than the kinematic temperature or (and more likely) the absorbing matter has a high bulk velocity dispersion (1σ line of sight velocity dispersion $\Delta v \simeq 1.3 \times 10^8 \text{ cm s}^{-1}$). We have shown that this gas may be the same as that which is responsible for the observed photoelectric absorption.

Further X-ray observations of the nucleus of NGC 4258 are required to monitor the variability of the iron absorption and emission lines. Such observations should have higher sensitivity and better spectral resolution than those presented here, with the goal of clean separation of absorption and emission lines.

We thank Yuichi Terashima and Chris Reynolds for discussions. This research was supported by NASA through grants NAG 8-1027 and NAG 8-1755.

REFERENCES

- Abramowicz, M. A., Chen, X., Kato, S., Lasota, J., & Regev, O. 1995, *ApJ*, 438, L37
- Anders, E. & Grevesse, N. 1989, *Geochim. Cosmochim. Acta*, 53, 197
- Arnaud, K. A. 1996, in *ASP Conf. Ser. 101: Astronomical Data Analysis Software and Systems V*, Vol. 5, 17
- Arnaud, M. & Raymond, J. 1992, *ApJ*, 398, 394
- Behar, E. & Netzer, H. 2002, *ApJ*, 570, 165

- Blandford, R. D. & Begelman, M. C. 1999, MNRAS, 303, L1
- Boirin, L. & Parmar, A. N. 2003, ArXiv Astrophysics e-prints
- Brandt, W. N. & Schulz, N. S. 2000, ApJ, 544, L123
- Cecil, G., Wilson, A. S., & de Pree, C. 1995, ApJ, 440, 181
- Cecil, G., Wilson, A. S., & Tully, R. B. 1992, ApJ, 390, 365
- Davis, J. E. 2001, ApJ, 562, 575
- Fabbiano, G., Kim, D.-W., & Trinchieri, G. 1992, ApJS, 80, 531
- Fiore, F., Pellegrini, S., Matt, G., Antonelli, L. A., Comastri, A., della Ceca, R., Giallongo, E., Mathur, S., Molendi, S., Siemiginowska, A., Trinchieri, G., & Wilkes, B. 2001, ApJ, 556, 150
- Greenhill, L. J., Jiang, D. R., Moran, J. M., Reid, M. J., Lo, K. Y., & Claussen, M. J. 1995, ApJ, 440, 619
- Herrnstein, J. R., Moran, J. M., Greenhill, L. J., Diamond, P. J., Inoue, M., Nakai, N., Miyoshi, M., Henkel, C., & Riess, A. 1999, Nature, 400, 539
- Iwasawa, K. 2003, private communication
- Kallman, T. R. & McCray, R. 1982, ApJS, 50, 263
- Kotani, T., Ebisawa, K., Dotani, T., Inoue, H., Nagase, F., Tanaka, Y., & Ueda, Y. 2000, ApJ, 539, 413
- Krolik, J. H. & Kallman, T. R. 1984, ApJ, 286, 366
- Lee, J. C., Reynolds, C. S., Remillard, R., Schulz, N. S., Blackman, E. G., & Fabian, A. C. 2002, ApJ, 567, 1102
- Makishima, K., Fujimoto, R., Ishisaki, Y., Kii, T., Loewenstein, M., Mushotzky, R., Serlemitsos, P., Sonobe, T., Tashiro, M., & Yaqoob, T. 1994, PASJ, 46, L77
- Miyoshi, M., Moran, J., Herrnstein, J., Greenhill, L., Nakai, N., Diamond, P., & Inoue, M. 1995, Nature, 373, 127
- Murphy, E. M., Lockman, F. J., Laor, A., & Elvis, M. 1996, ApJS, 105, 369
- Nakai, N., Inoue, M., & Miyoshi, M. 1993, Nature, 361, 45

- Narayan, R., Igumenshchev, I. V., & Abramowicz, M. A. 2000, *ApJ*, 539, 798
- Narayan, R. & Yi, I. 1994, *ApJ*, 428, L13
- Parmar, A. N., Oosterbroek, T., Boirin, L., & Lumb, D. 2002, *A&A*, 386, 910
- Pietsch, W. & Read, A. M. 2002, *A&A*, 384, 793
- Pietsch, W., Vogler, A., Kahabka, P., Jain, A., & Klein, U. 1994, *A&A*, 284, 386
- Ptak, A., Serlemitsos, P., Yaqoob, T., & Mushotzky, R. 1999, *ApJS*, 120, 179
- Quataert, E. & Gruzinov, A. 2000, *ApJ*, 539, 809
- Reynolds, C. S., Nowak, M. A., & Maloney, P. R. 2000, *ApJ*, 540, 143
- Schulz, N. S. & Brandt, W. N. 2002, *ApJ*, 572, 971
- Sidoli, L., Oosterbroek, T., Parmar, A. N., Lumb, D., & Erd, C. 2001, *A&A*, 379, 540
- Spitzer, L. 1978, *Physical processes in the interstellar medium* (New York Wiley-Interscience, 1978)
- Terashima, Y., Iyomoto, N., Ho, L. C., & Ptak, A. F. 2002, *ApJS*, 139, 1
- Ueda, Y., Asai, K., Yamaoka, K., Dotani, T., & Inoue, H. 2001, *ApJ*, 556, L87
- Ueda, Y., Inoue, H., Tanaka, Y., Ebisawa, K., Nagase, F., Kotani, T., & Gehrels, N. 1998, *ApJ*, 492, 782
- Verner, D. A., Verner, E. M., & Ferland, G. J. 1996, *Atomic Data and Nuclear Data Tables*, 64, 1
- Verner, D. A. & Yakovlev, D. G. 1995, *A&AS*, 109, 125
- Vogler, A. & Pietsch, W. 1999, *A&A*, 352, 64
- Wilkes, B. J., Schmidt, G. D., Smith, P. S., Mathur, S., & McLeod, K. K. 1995, *ApJ*, 455, L13
- Wilson, A. S., Yang, Y., & Cecil, G. 2001, *ApJ*, 560, 689, (WYC)
- Yamaoka, K., Ueda, Y., Inoue, H., Nagase, F., Ebisawa, K., Kotani, T., Tanaka, Y., & Zhang, S. N. 2001, *PASJ*, 53, 179
- Yuan, F., Markoff, S., Falcke, H., & Biermann, P. L. 2002, *A&A*, 391, 139

Table 1. Chandra Observations of NGC 4258

Date of obs.	Frame-time (sec)	Exposure time ^a (sec)	Observed count rate (counts sec ⁻¹)	De-piled count rate (counts sec ⁻¹)
2000-03-08	0.4	1570	0.304 ± 0.014	0.304 ± 0.014
2000-04-17	3.2	13056	0.161 ± 0.004	0.43 ^b
2001-05-28	3.2	20214	0.143 ± 0.003	0.28 ^b
2001-05-29	0.4	6819	0.243 ± 0.006	0.243 ± 0.006

^aTotal good exposure time, taking into account the good time intervals and dead-time correction factor.

^bThese count rates are subject to increased errors (see section 4).

Table 2. Continuum Spectral Models^a of the Nucleus of NGC 4258.

Date of obs.	kT_l (keV)	L_l^b (erg s ⁻¹)	N_H^c (cm ⁻²)	Γ_h	kT_h (keV)	L_h^d (erg s ⁻¹)	χ^2 / dof
2000-03-08	n/a	n/a	$6.9_{-1.8}^{+2.2} \times 10^{22}$	$1.3_{-0.6}^{+0.6}$		1.2×10^{41}	27 / 26
2000-04-17 ^e	$1.3_{-0.9}^{+\infty}$	1.6×10^{38}	$7.2_{-0.4}^{+0.7} \times 10^{22}$	$1.5_{-0.0}^{+0.1}$		1.3×10^{41}	113 / 103
2001-05-28 ^e	$1.3_{-0.8}^{+\infty}$	1.4×10^{38}	$6.5_{-0.3}^{+0.6} \times 10^{22}$	$1.5_{-0.1}^{+0.1}$		7.9×10^{40}	158 / 143
2001-05-29	$1.0_{-0.7}^{+0.6}$	1.5×10^{38}	$6.8_{-1.0}^{+1.2} \times 10^{22}$	$1.4_{-0.3}^{+0.3}$		7.4×10^{40}	105 / 93
2001-05-29	$0.9_{-0.3}^{+0.4}$	1.5×10^{38}	$6.5_{-0.5}^{+0.9} \times 10^{22}$		$58_{-41}^{+\infty}$	7.3×10^{40}	106 / 93

^aModel = [Galactic absorption] \times ([bremsstrahlung] + [intrinsic absorption] \times { [power law] *or* [bremsstrahlung] }). The subscript l refers to parameters of the low energy component, modeled as bremsstrahlung emission. The subscript h refers to the parameters of the high energy component, modeled as either a power-law or bremsstrahlung emission.

^b0.5–2 keV luminosity of the low-energy bremsstrahlung component, corrected for Galactic absorption.

^cIntrinsic equivalent hydrogen column density.

^d2–10 keV luminosity of the high-energy power-law or bremsstrahlung component, corrected for intrinsic and Galactic absorption.

^eResults corrected for the effects of pile-up.

Table 3. Iron Line Parameters for the Nucleus of NGC 4258

Date of obs.	Line energy (keV) ^a	Equivalent Width (eV) ^b		
	90% conf.	90% conf.	99% conf.	99.5% conf.
2000-03-08	6.40 ^c	–240 < EW < 887		
2000-04-17	6.41 ^{+0.05} _{–0.06}	–166 ⁺⁶² _{–100}	–166 ⁺¹⁰⁸ _{–110}	–166 ⁺¹¹⁵ _{–138}
2000-04-17	6.87 ^{+0.09} _{–0.06}	–215 ⁺¹¹⁵ _{–123}	–215 ⁺¹⁸² _{–186}	–215 ⁺¹⁹⁹ _{–203}
2000-04-17 (0 – 6 ksec) ^d	6.36 ^{+0.15} _{–0.13}	–105 ⁺¹⁰⁴ _{–79}		
2000-04-17 (0 – 6 ksec) ^d	6.95 ^{+0.22} _{–0.12}	–450 ⁺¹⁷² _{–280}	–450 ⁺²⁸⁰ _{–396}	–450 ⁺³⁰⁶ _{–413}
2000-04-17 (6 – 12 ksec) ^d	6.44 ^{+0.10} _{–0.16}	–249 ⁺¹⁴⁷ _{–205}	–249 ⁺¹⁶² _{–290}	–249 ⁺²⁰⁹ _{–293}
2000-04-17 (6 – 12 ksec) ^d	6.97 ^c	–208 < EW < 323		
2001-05-28	6.40 ^c	–41 < EW < 132		
2001-05-29	6.40 ^c	–72 < EW < 94		

^aMeasured in the rest frame of NGC 4258.

^bPositive values of EW indicate emission and negative values of EW indicate absorption.

^cParameter fixed.

^dThe 2000-04-17 observation has been split into two consecutive segments each of 6 ksec duration as indicated in parentheses.

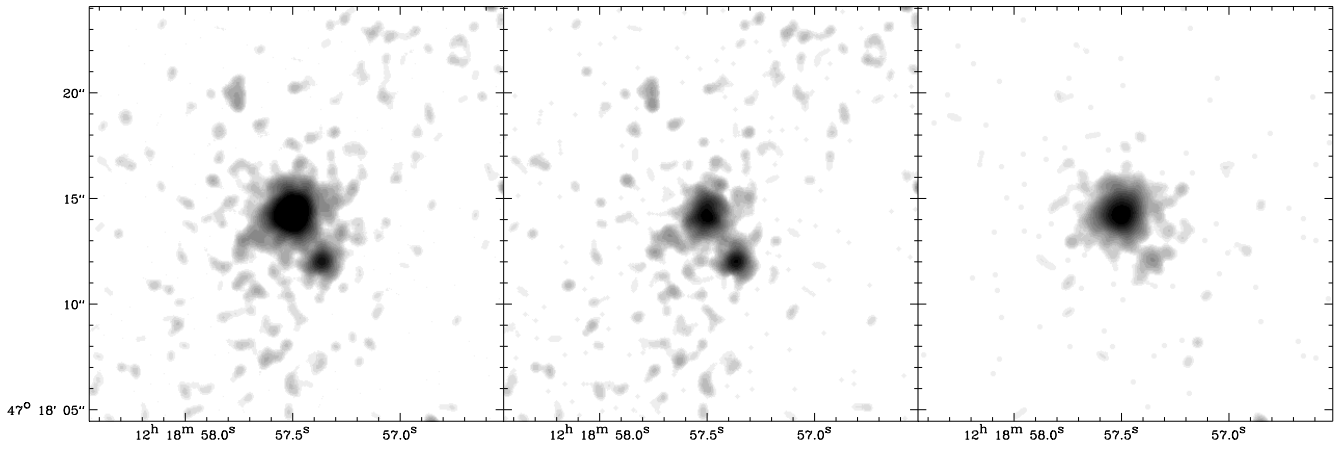


Fig. 1.— Grey scale representations of Chandra X-ray images of the nucleus of NGC 4258 in the energy bands 0.5 – 8 keV (left), 0.5 – 3 keV (center) and 3 – 8 keV (right). The images show the combined 3.2 sec frame-time data from the 13 ksec Cycle 1 and 20 ksec Cycle 2 observations. The images have been re-sampled to ten times smaller pixel size and smoothed by a Gaussian of FWHM 0".5.

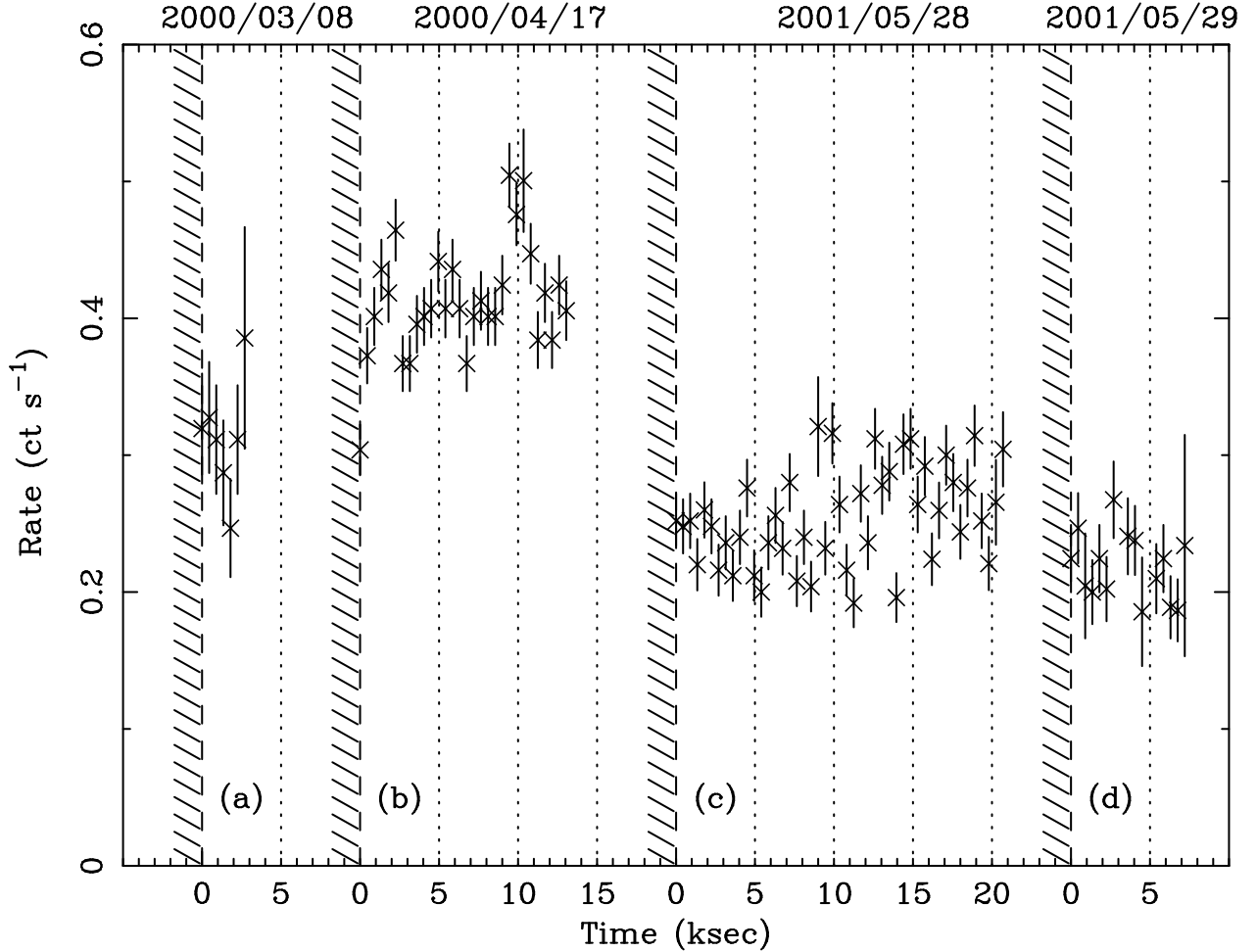


Fig. 2.— X-ray light curves from circular apertures of radius $1''.5$ centered on the nucleus of NGC 4258 in 450 s bins, from (a) the 1.6 ks 0.4 sec frame-time observation (left), (b) the 13 ks 3.2 sec frame-time observation (center left), (c) the 20 ksec 3.2 sec frame-time observation (center right), and (d) the 7 ksec 0.4 sec frame-time observation (right). Vertical dotted lines are placed every 5 ksec, and the shaded regions indicate the start of a new observation. The 3.2 sec frame-time data sets, (b) and (c), have been corrected for the effects of pile-up. The background count rate is negligible ($< \text{few} \times 10^{-4} \text{ cts s}^{-1}$). The error bars show the statistical noise, but do not include the systematic error associated with the pile-up correction of data sets (b) and (c).

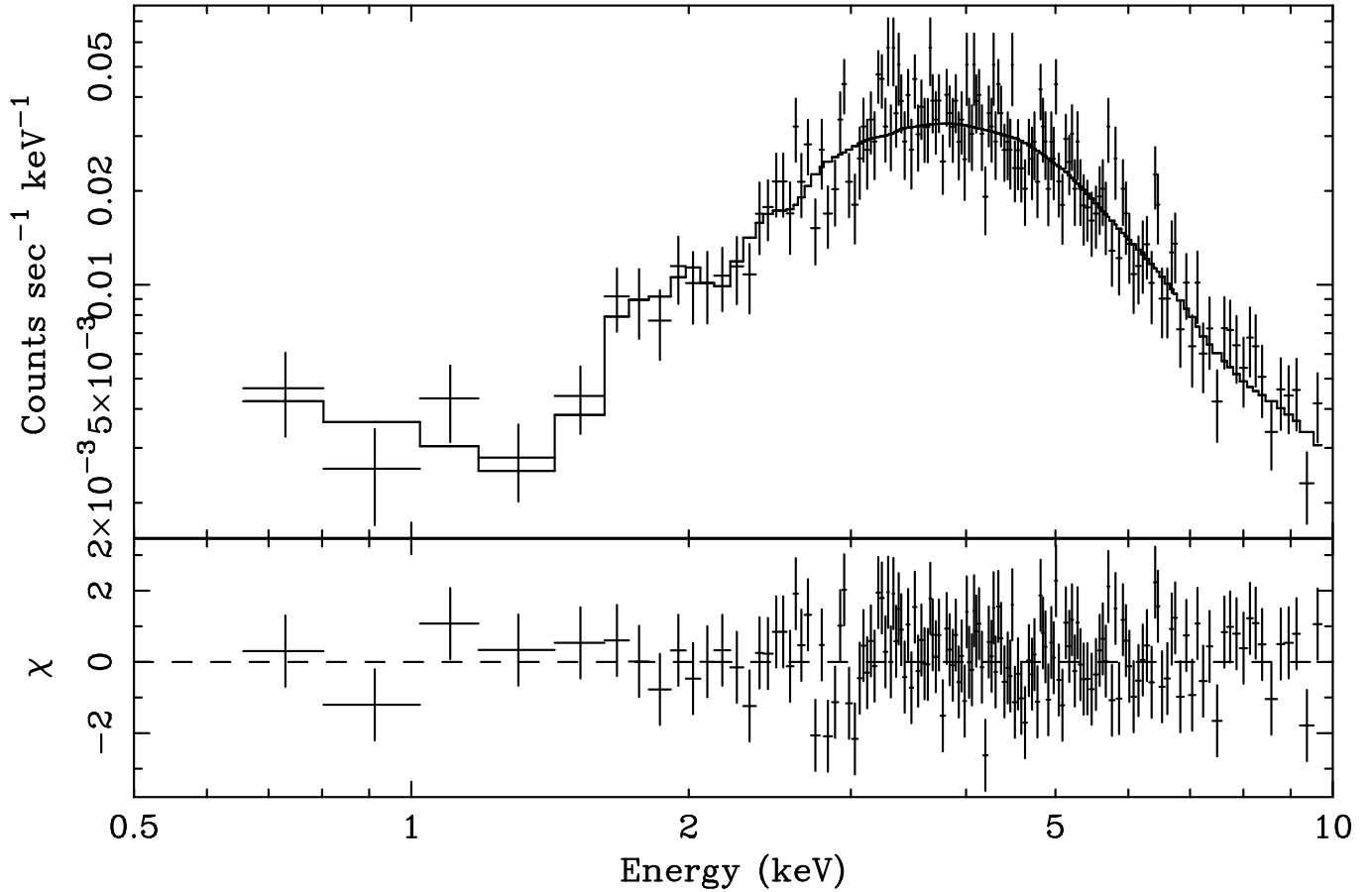


Fig. 3.— X-ray spectrum of the nucleus of NGC 4258 extracted from the 20 ksec observation of 2001-05-28. The upper panel shows data points with error bars (crosses), with the model folded through the instrument response, taking into account the effects of pile-up (solid line). The lower panel shows the χ residuals to this fit. The parameters of this model are listed in Table 2.

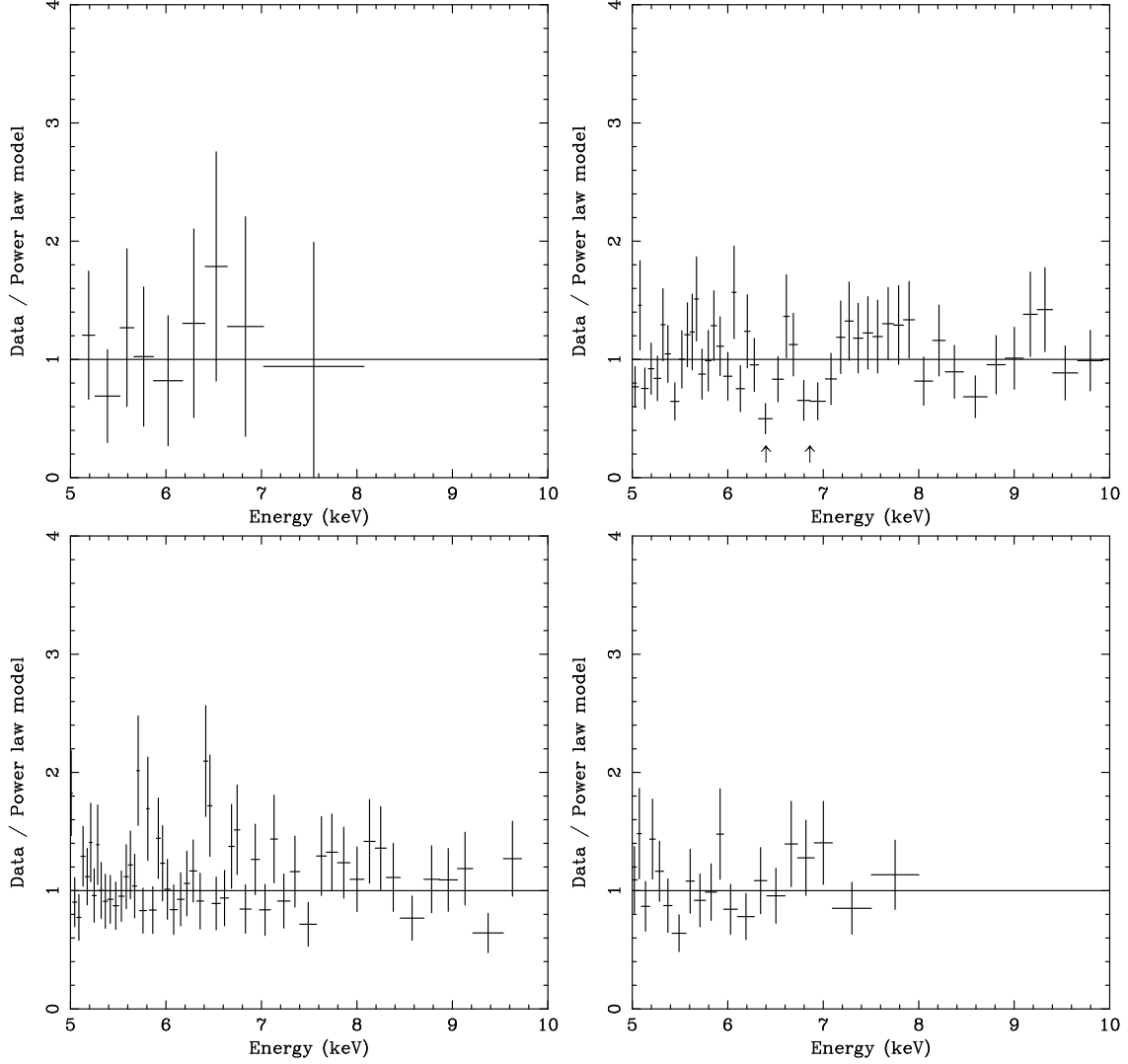


Fig. 4.— Chandra spectra of the nucleus of NGC 4258 including the Fe $K\alpha$ line region. Observations were made on 2000-03-08 for 1.6 ksec with a 0.4 sec frame-time (upper left panel), 2000-04-17 for 13 ksec with a 3.2 sec frame-time (upper right panel), 2001-05-28 for 20 ksec with a 3.2 sec frame-time (lower left panel) and 2001-05-29 for 7 ksec with a 0.4 sec frame-time (lower right panel). The spectra are grouped to have ≥ 15 cts bin^{-1} and the energy scale is as observed. The plots show the ratio of the data to the best fitting absorbed power law model above 5 keV. There is no evidence of strong Fe $K\alpha$ emission. On 2000-04-17, statistically significant absorption features are seen at 6.4 keV and 6.9 keV and are indicated by the arrows in the upper right panel.

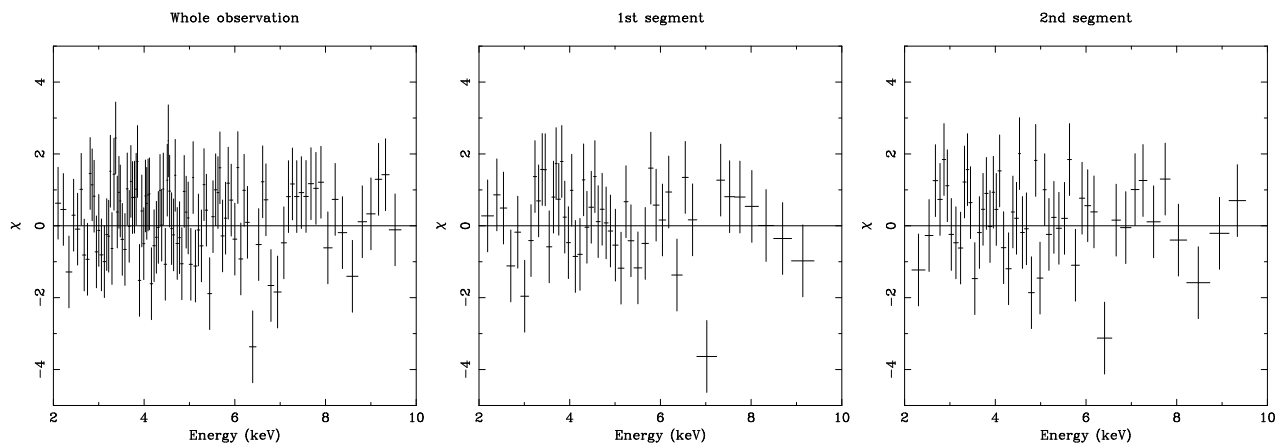


Fig. 5.— Chandra spectra of the nucleus of NGC 4258 covering the Fe $K\alpha$ line region from the 2000-04-17 13 ksec observation. The figures show the residuals, in terms of χ , from a power law model for the entire observation (left panel), the first 6000 sec segment of the observation (center panel) and the second 6000 sec segment of the observation (right panel). The presence of a strong absorption feature at 6.9 keV in the first segment is highly significant (at $> 99.5\%$ confidence), as is its disappearance in the subsequent segment. The 6.4 keV absorption line is marginally stronger in the second segment, where its presence is significant at $> 99.5\%$ confidence. The absorption line parameters for each panel are given in Table 3.

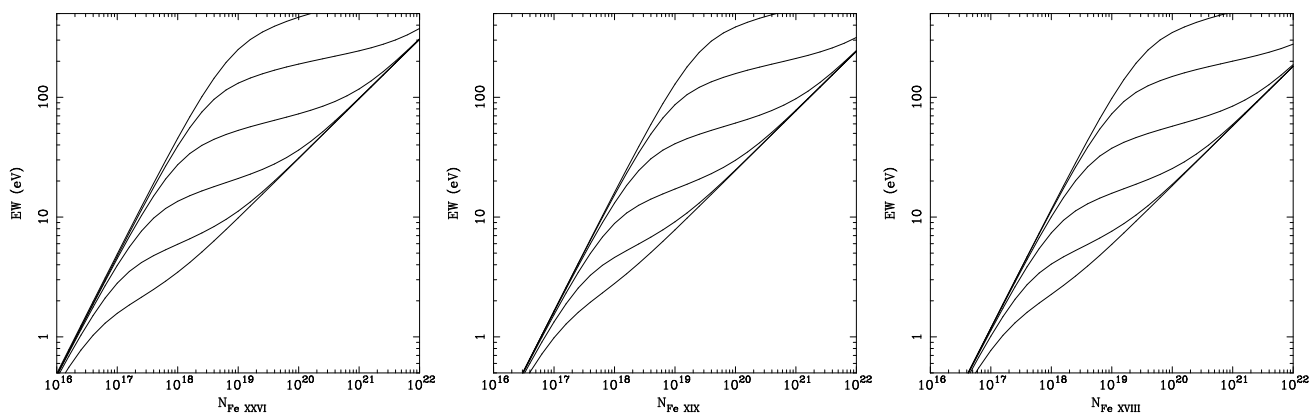


Fig. 6.— Curves of growth for Fe XXVI $K\alpha$ (left panel), Fe XIX $K\alpha$ (center panel) and Fe XVIII $K\alpha$ (right panel). The curves in each panel correspond to kinematic temperatures of 10,000 keV, 1000 keV, 100 keV, 10 keV, 1 keV and 0.1 keV, from top to bottom, respectively. The 1σ line of sight velocity dispersion of the iron ions is $\Delta v \sim 4.1 \times 10^8 \text{ cm s}^{-1}$ at 10,000 keV and $\Delta v \sim 1.3 \times 10^6 \text{ cm s}^{-1}$ at 0.1 keV.